Ni-doping influence on functional properties of $SrTi_{0.65}Fe_{0.35}O_{3-\delta}$ for use as oxygen transport membranes

Yuning Tang [a,b,c,*], Stefan Baumann [a,c], Michael Müller [a], Doris Sebold [a,c], Arian Nijmeijer [b], Olivier Guillon [a,c], Wilhelm A. Meulenberg [a,b,c]

[a] Forschungszentrum Jülich GmbH, Institute of Energy Materials and Devices (IMD), Jülich 52425, Germany
[b] Inorganic Membranes, Faculty of Science and Technology, University of Twente, P.O. Box 217, Enschede 7500 AE, the Netherlands
[c] Jülich Aachen Research Alliance: JARA-Energy, Jülich 52425, Germany

ARTICLE INFO

ABSTRACT

Pure strontium titanate, $SrTiO_3$, exhibits excellent thermodynamic stability but negligible electronic and ionic conductivity in a wide range of temperatures and oxygen partial pressures. In order to improve the conductivity, B-site doping strategy is used in this work. The $SrTi_{0.65-x}Fe_{0.35}Ni_xO_{3-\delta}$ (x=0, 0.05, 0.075, 0.1) (STFN$_x$) powders were synthesized by a solid-state reaction method at 1200 °C and then sintered into membranes at 1350/1400 °C for 5 h. Functionality, i.e. mixed ionic and electronic conductivity, is introduced by substitution of Ti by Fe and Ni. In addition, Ni is proven to improve the catalytic performance by exsolution phenomenon. The XRD patterns show that the materials are single phase after sintering in air. The oxygen permeance and the ionic conductivity of STFN$_x$ increase with an increasing Ni content and are close to benchmark $La_{0.6}Sr_{0.4}Co_{0.2}Fe_{0.8}O_{3-\delta}$ at around 850 °C. Thermochemical stability tests were performed by annealing samples in syngas with/without H$_2$S and clean H$_2$. XRD analysis and thermogravimetry analysis (TGA) reveal that STFN005 exhibits good thermochemical stability in reducing atmospheres and the stability of STFN$_x$ decreases with increasing Ni content. Well distributed Fe/Ni exsolution particles can be found even with the lowest Ni amount doped material $SrTi_{0.6}Fe_{0.35}Ni_{0.05}O_{3-\delta}$ after annealing in reducing atmosphere, which will be beneficial to catalytic performance in a membrane reactor. Therefore, 5 % Ni doped STFN005 can be a promising material in catalytic membrane reactors, e.g. for partial oxidation of methane (POM).

1. Introduction

Mixed ionic-electronic conducting (MIEC) materials are promising candidates of oxygen transport membranes (OTMs). They have attracted great interests in scientific research due to the high product purity and energy efficiency of oxygen separation from air as well as application in catalytic membrane reactors, e.g. for partial oxidation of methane (POM) [1,2] and solid oxide fuel cell (SOFC) electrodes [3,4]. For membrane reactors, materials are usually operated under harsh reducing and/or corrosive atmosphere like CO, H$_2$ and CH$_4$ at high temperature of approx. 800–900 °C. Therefore, the structural stability of MIEC membranes under operating conditions is a very important factor. $La_{1-x}Sr_xCo_{1-y}Fe_yO_{3-\delta}$ (LSCF) and $Ba_{0.5}Sr_{0.5}Co_{0.8}Fe_{0.2}O_{3-\delta}$ (BSCF) have been widely studied showing high oxygen permeability [5–12]. However, the high oxygen permeability of LSCF and BSCF relies on highly redox-active B-site elements in particular Co, which is accompanied

with low structural stability in reducing environments [9–12]. Some approaches have been applied for improving the stability of MIEC membranes. For example, partial substitution of A or B sites with cations with a higher valence or larger radius, such as Al [13,14], Ti [15], Zr [16], Y [17,18] and Nb [19]. Although these methods successfully improved stability to some degree, these materials are still not sufficiently stable against the reducing and corrosive atmospheres in some membrane reactors due to the high amount of Co and Fe on the B-site. Besides, the substitution of Co/Fe with Al/Zn will also reduce the oxygen permeability and conductivity in some cases due to lower oxygen diffusion or much lower oxygen surface-exchange kinetics[20,21] In addition, dual-phase ceramic membranes have also shown to be stable for the use in membrane reactors by introducing fluorites such as Y doped ZrO$_2$ (YSZ), Sm$_2$O$_3$ doped CeO$_2$ (SDC) or Gd doped CeO$_2$ (GDC) into the material structure [22,23]. However, stability issues in reducing atmospheres remain due to the redox-active electronic conducting

second phase as well as the chemical expansion particularly of ceria and resulting thermal/chemical stresses in the composite.

On the other hand, the perovskite material $SrTiO_3$ exhibits high stability in a wide range of temperatures and atmospheres, but negligible oxygen permeation performance due to a low concentration of intrinsic defects. The performance of $SrTiO_3$ can be improved by A/B-site doping strategies to create oxygen vacancies as well as electronic defects in the material. In particular, B-site Ti^{4+} can be substituted by metal cations with lower valence, such as Fe^{3+}[24–27], Co^{2+}[28,29], Al^{3+}[30,31], Mg^{2+}[32] and Ni^{2+}[33,34], in order to introduce the required oxygen permeability. Redox-active elements, i.e. Fe, Co and in particular Ni, can be exsolved from the crystal lattice in very reducing atmospheres [33,35–37]. Since Ni-based catalysts can achieve good CH_4 conversion and syngas selectivity in partial oxidation of methane (POM), Ni is a promising dopant potentially improving both the permeability as well as the catalytic activity. Our preliminary work indicated that $SrTi_{0.65}Fe_{0.35}O_{3-\delta}$ (STF35) can achieve a good balance between stability and oxygen separation from air while Co doping again leads to instability in reducing atmospheres [24,38]. However, the influence of Ni-doping on the functional properties of STF35 for oxygen transport membrane (OTM) materials has not yet been systematically characterized. Therefore, we studied the compositions $SrTi_{0.65-x}Fe_{0.35}Ni_xO_{3-\delta}$ (x=0, 0.05, 0.075, 0.1) (STFN$_x$) with the effects of Ni doping on oxygen permeation, electronic conductivity. The phase stability after annealing in H_2/Ar, clean syngas and syngas with H_2S contamination was also investigated.

2. Experimental

2.1. Sample preparation

$SrTi_{0.65-x}Fe_{0.35}Ni_xO_{3-\delta}$ (x=0, 0.05, 0.075, 0.1) (STF35, STFN005, STFN0075 and STFN010) powder was synthesized by a solid-state reaction method. The precursors $SrCO_3$ (Merck, 99 %), TiO_2 (Merck, 99 %), Fe_2O_3 (Merck, 99 %), NiO (Merck, 99 %) were ball milled for 24 h, dried and sieved through 500 μm mesh, then calcined at 1200 °C for 5 h. The derived powders were ball milled again for 24 h. As-synthesized powder was collected after drying. Bulk membranes were then uniaxially pressed in the form of discs at around 70 MPa for 1.5 minutes using an uniaxial press model PW10 (∅ 20 mm) (Fa. Paul Otto Weber GmbH, Remshalden). The pressed STFN$_x$ and STF35 membranes were sintered at 1350 °C and 1400 °C for 5 h, respectively. Heating and cooling rates were 5 K/min.

2.2. Structural characterization

The desired composition of Sr, Ti, Fe, and Ni was confirmed by Inductively Coupled Plasma-Optical Emission Spectrometry (ICP-OES) on a Thermo Scientific™ iCAP™ 7600 ICP-OES Analyzer. The particle size distribution (PSD) of the powder was determined using a particle analyzer HORIBA LA-950V2 (Horiba European GmbH, Germany). Crystalline structure and phase compositions were tested by X-ray diffraction (XRD) using a Bruker D4 ENDEAVOR diffractometer at room temperature with Cu Kα radiation in the 2θ range 10–80º. The step size used was 0.02° and 0.75 s per step. The XRD patterns were analyzed using Topas software. Microstructures were imaged via scanning electron microscopy (SEM) using a Zeiss GeminiSEM 450. Energy dispersive X-ray spectroscopy (EDS) was performed with Ultim Max 170 detector from Oxford Instruments. The gas tightness of the sintered membrane was checked by a He-leak rate detector (Qualy test HTL 260, Pfeiffer Vacuum GmbH, Asslar, Germany). The cyclic thermogravimetric analysis (TGA) measurements were carried out with a calorimeter STA449 F1 Jupiter coupled to the mass spectrometer QMS 403 C Aëolos (Netzsch) in air and 2.9 % H_2/Ar. The final temperature was 900 °C with a heating/cooling rate of 10 °C/min in air and the gas flow rate was 50 mL/min. The holding time was 2 h for every cycle for reduction as well as oxidation.

2.3. Electrical conductivity measurements

Temperature dependent electrical conductivity measurements were conducted on a Keithley 2400 four-probe DC measurement setup from 600 to 900 °C in air (21 % O_2 and 79 % N_2). All samples were ground with sand paper step by step in order to remove contaminations on the surface and get a smooth surface before measurements. With a diamond wire saw (HDS25, Diamond WireTec GmbH&Co.KG), the samples were cut into bars with approx. 6 mm width, 15 mm length and 0.7 mm height. Gold wires with a diameter of 0.25 mm were used to connect the rectangular samples with the DC measurement setup and additional gold paste was also used to enhance the contact between the gold wires and the sample surface. The total electrical conductivity of the materials can be calculated using the following equation:

$$\sigma_{total} = \frac{D}{R \cdot A} \tag{1}$$

where σ_{total} is the total electrical conductivity (S/cm), D is the distance between the inner voltage electrodes (cm), R is the resistance (Ω) and A is the cross-sectional area of the rectangular samples (cm^2), respectively.

2.4. Oxygen permeation measurement

The oxygen permeance is an important parameter to investigate the performance of oxygen transport membranes. It can be calculated by normalizing the oxygen permeation flux j(O_2) by the oxygen partial pressure gradient ($\ln \frac{P'_{O_2}}{P''_{O_2}}$), which is the driving force for oxygen permeation. The oxygen permeation flux j(O_2) can be expressed by Eq. (2):

$$j(O_2) = \frac{R}{16F^2 \cdot L} \cdot T \cdot \sigma_{amb} \cdot \ln \frac{P'_{O_2}}{P''_{O_2}} \tag{2}$$

where R is the gas constant, T is the temperature, F is the Faraday constant, L is the thickness of the membrane, P'_{O_2} and P''_{O_2} are the oxygen partial pressure of oxygen rich and lean side of the membrane, respectively, and σ_{amb} is the ambipolar conductivity, which can be expressed by Eq. (3):

$$\sigma_{amb} = \frac{\sigma_i \cdot \sigma_e}{\sigma_i + \sigma_e} \tag{3}$$

where σ_i and σ_e are the ionic and electronic conductivity, respectively.

The oxygen permeance can be expressed as:

$$Permeance = \frac{j(O_2)}{\ln \frac{P'_{O_2}}{P''_{O_2}}} = \frac{R}{16F^2 \cdot L} \cdot T \cdot \sigma_{amb} \tag{4}$$

The activation energy of the oxygen permeance can be obtained by the Arrhenius approach:

$$\ln\left(permeance\right) = -\frac{Ea}{RT} + A \tag{5}$$

Where E_a ist the activation energy and A is the pre-exponential factor.

Oxygen permeation measurements were conducted on a 4-end mode set up in air (feed gas)/Ar (sweep side) atmosphere from 650 °C to 1000 °C. The size of the dense membrane was around ∅ 14.6 mm x 1 mm. The flow rate of the gas streams was controlled using mass flow controllers (MFCs). The standard flow rate was 250 mL·min^{-1} for the feed side (air) and 50 mL·min^{-1} for the sweep side (Ar). All samples were ground to 1 mm thickness using the same process for electrical conductivity measurements. Afterwards, the samples were sealed using gold rings with an inner diameter of 13 mm to a quartz glass reactor. The O_2 concentration was recorded by a mass spectrometer (Omni Star, Pfeiffer

Table 1

Particle size distribution of as-synthesized powders and sintering temperature of the samples.

| Name	Composition	d10 μm	d50 μm	d90 μm	Sintering temperature (°C)
STF35	$SrTi_{0.65}Fe_{0.35}O_{3-\delta}$	0.84	1.68	3.87	1400
STFN005	$SrTi_{0.6}Fe_{0.35}Ni_{0.05}O_{3-\delta}$	0.80	1.44	3.04	1350
STFN0075	$SrTi_{0.575}Fe_{0.35}Ni_{0.075}O_{3-\delta}$	0.79	1.47	3.10	1350
STFN010	$SrTi_{0.55}Fe_{0.35}Ni_{0.1}O_{3-\delta}$	0.89	1.60	3.55	1350

vacuum US) during measurements.

2.5. Annealing measurement

The annealing experiments aimed to investigate the thermo-chemical stability of the materials by simulating the gas composition from partial oxidation of methane ($CH_4 + 0.5 O_2 => CO + 2 H_2$). To prevent the formation of soot even at the lowest temperature, steam was added in the mixed gas. Furthermore, clean methane and sour gas containing H_2S was considered. Therefore, the samples were annealed for 72 h in a gas stream of 150 mL/min 25 vol% CO (with/without 1000 ppm H_2S) + 50 vol% H_2 + 25 vol% H_2O forming different syngas compositions (pure syngas and syngas with H_2S) equilibrated at 600 °C, 700 °C, 800 °C, and 900 °C, respectively. Experiments were conducted in a four tubes set-up[39], which can anneal samples at four different temperatures in the same gas atmosphere at the same time. Sintered pellets (⌀ 8 mm×5 mm) were put in alumina boats in order to investigate the surface change before and after annealing. The well mixed gases were sent to the tubes when the four tubes reached the different aimed temperatures. The tubes were heated/cooled in N_2 with a rate of 10 K/min. The annealing experiment in clean H_2 was conducted in 2.9 % H_2/Ar at 800 °C for 10 h. The software package FactSage 7.1 (GTT
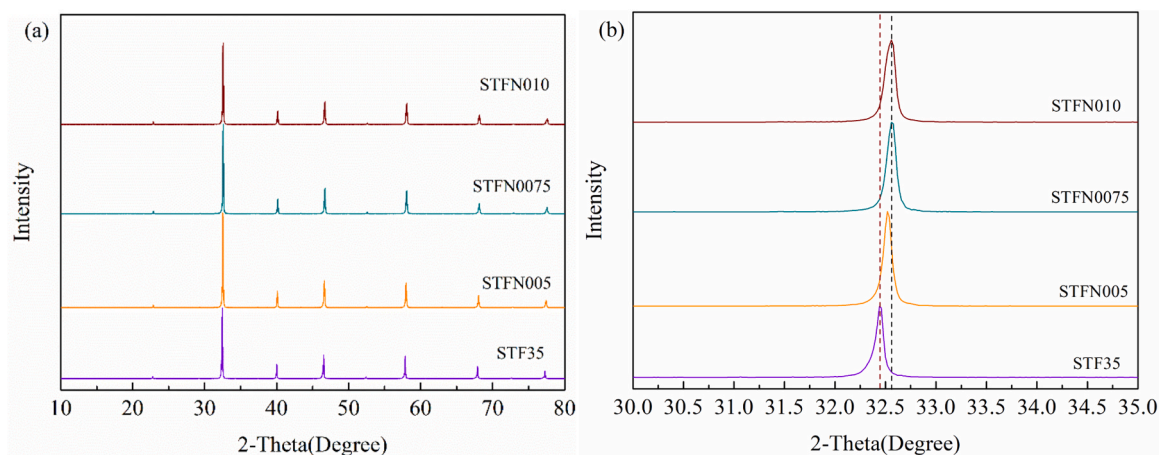
Fig. 1. XRD patterns of the sintered samples of STF35 and STFN$_x$.
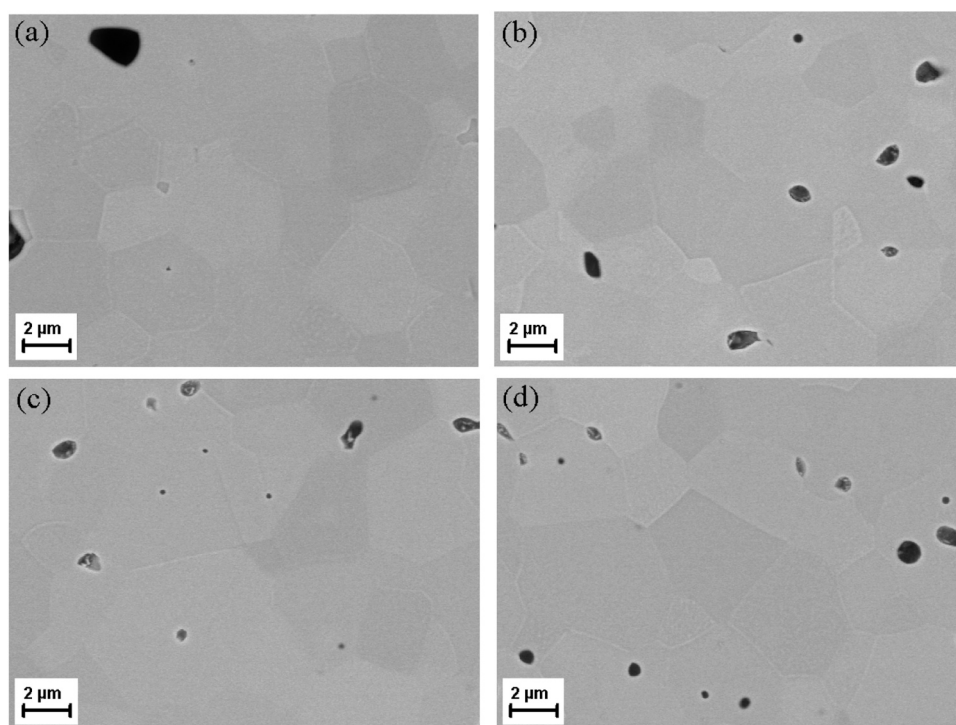
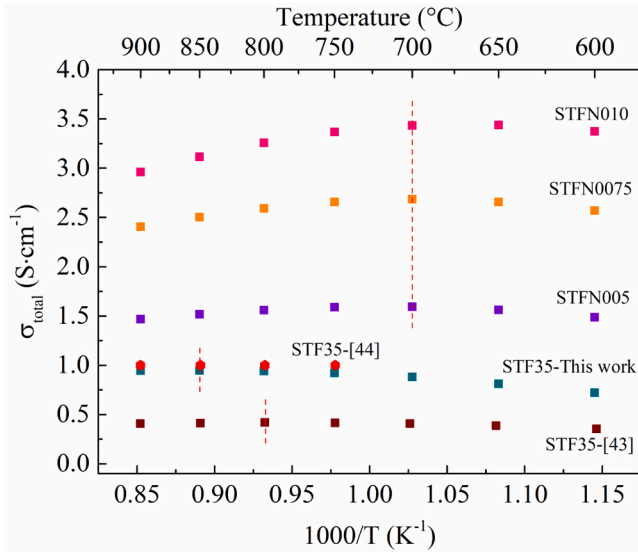**Fig. 2.** Cross-section of sintered (a) STF35; (b) STFN005; (C) STFN0075 and (D) STFN010.

Fig. 3. Total electrical conductivity of STF35 and STFN$_x$ in air.

Fig. 4. Permeance of STF35, STFN$_x$ and benchmark LSCF6428 [24] of 1 mm thickness.

Technologies, Herzogenrath, Germany) was used for thermodynamic calculations. The calculations were based on the commercial database FactPS in the software package.

3. Results and discussion

3.1. Crystal structure and microstructure

Table 1 lists the particle size distribution of as-synthesized powders after calcination and sieving and the sintering temperature of the pressed samples. The powders show a monomodal distribution with d50 values around 1.5 μm. The intended chemical composition of all samples was confirmed by ICP-OES measurements. Fig. 1(a) shows the XRD patterns of the STF35 and STFN$_x$ pellets sintered at 1400 °C and 1350 °C for 5 h, respectively, confirming that all pellets are single phase. The results identify that the space group of all the materials is Pm3m (cubic perovskite structure). Doping Ni in STF35 causes shifting of all reflections towards higher diffraction angles, exemplarily shown by zoomed-in patterns for 30°~35° (Fig. 1(b)), which indicates a decrease in the lattice constant. The lattice parameters of the perovskites have been determined from XRD patterns, which are 3.903 Å, 3.897 Å, 3.891 Å and 3.889 Å for STF35, STFN005, STFN0075 and STFN010, respectively. It was reported that Ni can take +2 (0.69 Å) and +3 (0.56 Å) oxidation states during incorporation into Ti in SrTiO$_3$ [40,41] and Ni-doped STF structures [34,42]. The substitution of the host Ti^{4+} (0.605 Å) with the dopant Ni^{3+} (0.56 Å) is expected to decrease the lattice constant of SrTi$_{1-x}$Ni$_x$O$_3$ [40,41]. Therefore, the observed lattice parameter changes of the STFN$_x$ materials suggest that the introduction Ni is most likely in the state of +3. In addition, STF-series and STC-series have also been studied that the lattice parameter of the materials decreased with Fe/Co content increased due to smaller ionic radii of Fe^{4+}/Co^{3+} (0.585 Å /0.545 Å) valence state compared with Ti^{4+} (0.605 Å) [24,28]. SEM images of cross-section of sintered pellets (Fig. 2) show that all the sintered materials exhibit good density, which is confirmed by Helium leakage experiments ($< 10^{-7}$ mbar·L·s^{-1}).

3.2. Functional properties

Electrical conductivity and oxygen permeation performance were measured to investigate the functional properties of all the materials.

Fig. 3 shows that the total electrical conductivity of STFN$_x$ increases with increasing Ni content in air and all compositions showed a similar temperature dependence. All materials exhibit semiconductive behavior
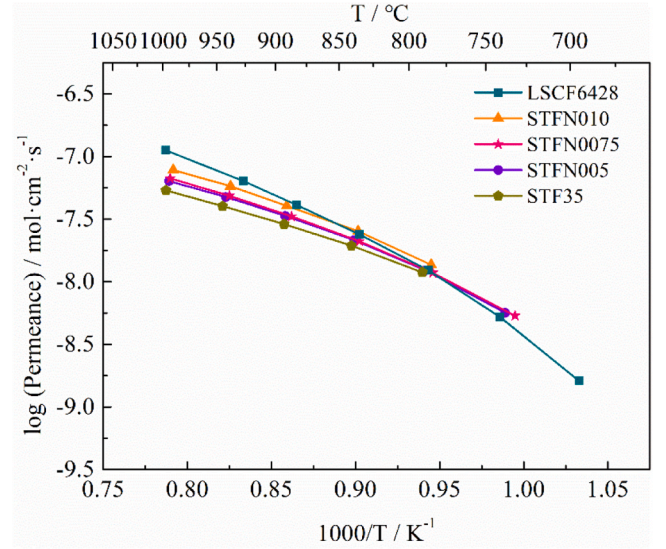
at low temperature, i.e. below 700 °C of STFN$_x$ (pink dash line), switching to metallic behavior at higher temperature, i.e. above 700 °C of STFN$_x$ (pink dash line) in the studied range, The measured conductivity of STF35 as well as the temperature dependence is reasonable compared to literature data [26,43–46]. In such semiconductive materials, the electron-lattice distortion coupling is weak at relative low temperature and the migration of small polarons is equivalent to electrons, resulting in rising conductivity with temperature. However, the mobility of small polaron hopping decreases due to strong electron–lattice distortion coupling at relative high temperature. Therefore, the migration of small polarons is lower than electrons, resulting in a decreasing conductivity with temperature[45].

Fig. 4 compared the permeance of 1 mm thick STF35, STFN$_x$, and LSCF6428 as a benchmark. The permeance and oxygen flux increases slightly with increasing Ni content due to the enhanced oxygen vacancy concentration. Furthermore, STFN010 exhibits a comparable permeation rate to the standard OTM material LSCF6428 [24] at around 850 °C, and is slightly higher at lower temperatures due to the lower activation energy. Table 2 lists the oxygen flux, permeance and activation energy Ea of LSCF6428, STF35, STFN$_x$ as well as the oxygen flux of other oxygen transport membranes at around 900 °C. Although these membranes [47–53]exist quite higher oxygen flux than STFNx, their stability in reducing atmospheres is still too low to meet the requirements in a membrane reactor.

The ionic conductivity σ$_i$ can be estimated by calculated the respective ionic transference number t$_i$ according to Eqs. (6–8).
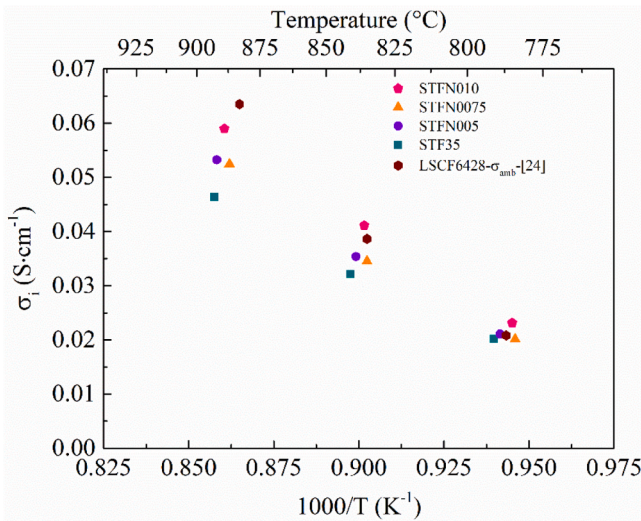
$$\sigma_{total} = \sigma_i + \sigma_e \tag{6}$$

$$\frac{\sigma_{amb}}{\sigma_{total}} = t_i \left(1 - t_i \right) \tag{7}$$

$$\sigma_i = \sigma_{total} \cdot t_i \tag{8}$$

As the ionic transference number of LSCF6428 is quite low 9×10^{-4} at 900 °C [54], and thus, the ionic conductivity is approx. equal to the ambipolar conductivity published by the literature [24] based on permeation tests. The ionic conductivity of different materials is plotted in Fig. 5. The ionic conductivity of STFN$_x$ is comparable with benchmark LSCF6428 and it increased with increasing Ni content. The activation energy Ea was calculated according to the Arrhenius Eq. (8):

Table 2

Oxygen flux, permeance and activation energy Ea of LSCF6428, STF35, STFN$_x$ and other oxygen transport membranes at around 900 °C.

Composition	T °C	Oxygen flux mL·cm^{-2}·min^{-1}	Log (Permeance) mol·cm^{-2}·s^{-1}	Ea of Permeance (800–1000 °C) kJ/mol	Thickness (mm)	Ref.
SrTi$_{0.65}$Fe$_{0.35}$O$_{3-\delta}$ (STF35)	893	0.15	-7.40	82	1	This work
SrTi$_{0.6}$Fe$_{0.35}$Ni$_{0.05}$O$_{3-\delta}$ (STFN005)	892	0.17	-7.32	89	1	This work
SrTi$_{0.575}$Fe$_{0.35}$Ni$_{0.075}$O$_{3-\delta}$ (STFN0075)	887	0.17	-7.31	92	1	This work
SrTi$_{0.55}$Fe$_{0.35}$Ni$_{0.1}$O$_{3-\delta}$ (STFN010)	889	0.20	-7.24	86	1	This work
La$_{0.6}$Sr$_{0.4}$Co$_{0.2}$Fe$_{0.8}$O$_{3-\delta}$ (LSCF6428)	883	0.20	-7.19	118	1	[24]
CaTi$_{0.73}$Fe$_{0.18}$Mg$_{0.09}$O$_{3-\delta}$-	900	0.46	-	-	0.9	[47]
BaFe$_{0.8}$Ca$_{0.05}$Ti$_{0.15}$O$_{3-\delta}$	900	0.87	-	-	1	[48]
SrCo$_{0.9}$Nb$_{0.1}$O$_{3-\delta}$	900	4.24	-	-	1	[49]
SrCo$_{0.8}$Sc$_{0.2}$O$_{3-\delta}$	900	3.09	-	-	1	[50]
Ba$_{0.6}$Sr$_{0.4}$Co$_{0.7}$Fe$_{0.25}$Bi$_{0.05}$O$_{3-\delta}$	900	1.05	-	-	1.2	[51]
BaCo$_{0.7}$Fe$_{0.15}$In$_{0.15}$O$_{3-\delta}$	900	1.30	-	-	1	[52]
SrCo$_{0.1}$Fe$_{0.8}$Nb$_{0.1}$O$_{3-\delta}$	900	0.9	-	-	1	[53]

Fig. 5. Ionic conductivity of different materials in air.

Table 4

Equilibrium gas composition during annealing measurement in pure syngas.

Composition	600 °C	700 °C	800 °C	900 °C
H$_2$	47.05 %	56.00 %	56.40 %	55.45 %
CO	8.87 %	15.86 %	18.33 %	19.51 %
H$_2$O	24.13 %	18.37 %	18.54 %	19.54 %
CO$_2$	12.31 %	8.51 %	6.62 %	5.48 %
CH$_4$	7.63 %	1.25 %	0.11 %	0.01 %
O$_2$(atm)	3.46E-25	1.56E-22	4.73E-20	6.27E-18

Table 5

Equilibrium gas composition during annealing measurement in syngas with H$_2$S.

Composition	600 °C	700 °C	800 °C	900 °C
H$_2$	47.06 %	55.99 %	56.38 %	55.44 %
CO	8.83 %	15.79 %	18.25 %	19.43 %
H$_2$O	24.14 %	18.39 %	18.56 %	19.56 %
CO$_2$	12.25 %	8.48 %	6.60 %	5.46 %
CH$_4$	7.60 %	1.25 %	0.11 %	0.01 %
H$_2$S(ppm)	1145	1016	992	989
Lg(p(H$_2$S))(atm)	-2.94	-2.99	-3.00	-3.00
O$_2$(atm)	3.44E-25	1.54E-22	4.69E-20	6.23E-18

Table 3

Ionic conductivity, electronic conductivity, ionic transference number t_i and activation energy Ea of STF35 and STFN$_x$ at around 900 °C.

| Name	T °C	Ionic Conductivity S·cm^{-1}	Electronic conductivity S·cm^{-1}	Ionic transference number t_i	Ea (800–900 °C) kJ/mol
STF35	893	4.64×10^{-2}	0.925	5.02×10^{-2}	84
STFN005	892	5.31×10^{-2}	1.468	3.62×10^{-2}	93
STFN0075	887	5.29×10^{-2}	2.406	2.20×10^{-2}	95
STFN010	889	5.90×10^{-2}	2.961	1.99×10^{-2}	92

$$\sigma_t = \sigma_0 \cdot \exp\left(-\frac{1}{T}\cdot\frac{Ea}{R}\right) \tag{9}$$

The results reveal that the activation energy Ea of STF35 and STFN$_x$ is in the range 84–95 kJ·mol^{-1} (Table 3), which is lower than that of LSCF6428 (103 kJ·mol^{-1}) [24]

3.3. Thermo-chemical stability

Annealing and Two-cycle TGA measurements were conducted to study the thermo-chemical stability of all the materials.

The phase composition of the STF35 and STFN$_x$ samples after
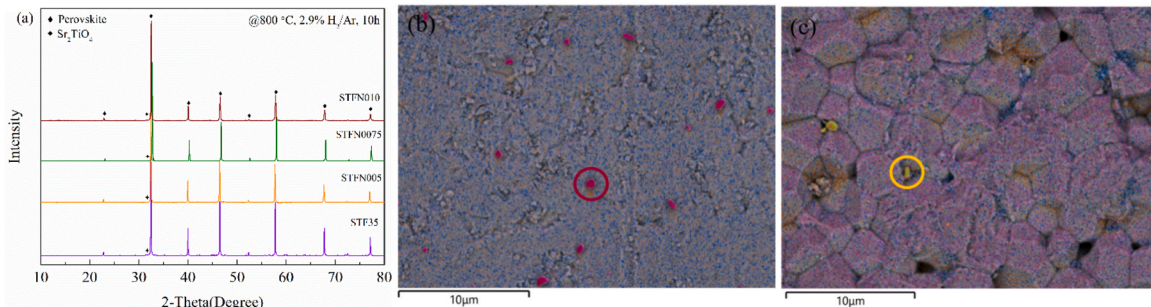
Fig. 6. (a) XRD patterns, SEM image with EDS-spectrum of (b) STF35 and (c) STFN005 after annealing in 2.9 % H$_2$/Ar at 800 °C.
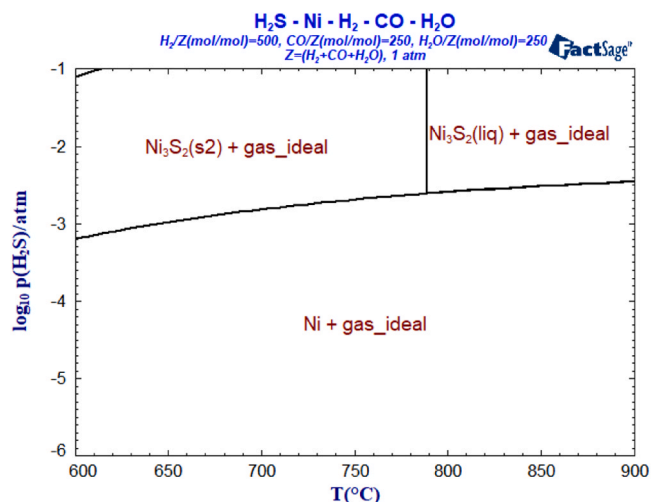
Fig. 7. Stability of Ni compounds at different temperatures and H_2S partial pressures in syngas.

annealing under different conditions, i.e. clean H_2, pure syngas, and syngas with H_2S was measured. XRD patterns of sintered pellets annealed in 2.9 % H_2/Ar at 800 °C for 10 h (Fig. 6(a)) reveal that minor Ruddlesden-Popper-like phases Sr_2TiO_4 have formed. Potential exsolution of Ni and Fe [33,37] cannot be detected by XRD due to too low sensitivity. Therefore, the surface of annealed samples was analyzed by SEM/EDS. Fig. 6(b-c) shows exemplarily STF35 and STFN005 confirming the exsolution phenomenon. Fe particles marked in pink are well-dispersed on the STF35 surface as shown in Fig. 6(b) and Fe/Ni

inter-metallic phase can be found even with the lowest Ni-doped amount material STFN005 surface marked by the yellow circle in Fig. 6(c).

Table 4 and Table 5 list the calculated gas composition at different temperatures during annealing measurements in pure syngas and syngas with H_2S, respectively. It is assumed that all gas components reach equilibrium during measurements due to the relatively long residence time at respective temperatures. The oxygen partial pressure increases with temperature. The slight changes in H_2S concentration originate from the gas phase reactions resulting in slightly different gas volume (e. g. $CO + 3 H_2 => CH_4 + H_2O$; 4 mol => 2 mol). From thermodynamic calculations, potentially ex-solved Ni is expected to equilibrate in presence of H_2S forming Ni_3S_2 (solid/liquid) depending on temperature as shown in Fig. 7. Unfortunately, STF is not present in the commercial database, so that its stability cannot be predicted by the FactSage software.

The XRD results of samples annealed in pure syngas show that the materials can maintain single phase after annealing in pure syngas below 700 °C (Fig. 8(a)). Additional peaks of $Sr_4Ti_3O_{10}$ and Fe/Ni metallic phase are detected at 900 °C as shown in Fig. 8(b). The decomposition of perovskite can be explained by the very low pO_2 (10^{-18} bar) and high temperature. Some of the Fe and Ni cations were reduced from the perovskite structure to the metallic state and were therefore extracted from the oxide lattice forming Fe/Ni metallic phase. In order to compensate for the loss of B-site cations, the remaining composition in the structure will form Sr-richer Ruddlesden-Popper-like phases $Sr_4Ti_3O_{10}$. Fig. 8(c) reveals that Fe/Ni (marked in yellow) are well distributed on the surface of STFN005 annealed at 900 °C in pure syngas. This will potentially enhance the catalytic performance in a membrane reactor in particular for (partial) oxidation reactions.

For the materials annealed in syngas with H_2S, all the samples are still stable at 600 °C (Fig. 9(a)). Nevertheless, the Fe/Ni exsolution
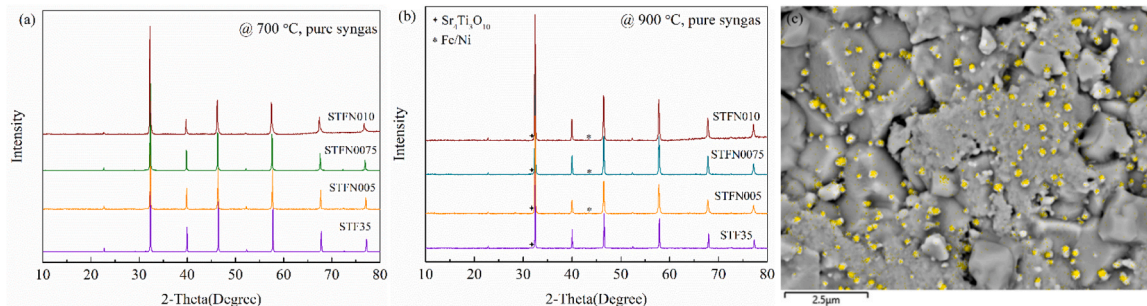

Fig. 8. XRD patterns of samples annealed at (a) 700 °C and (b) 900 °C, (c) SEM image with EDS-spectrum of Ni (in yellow) of STFN005 annealed at 900 °C in pure syngas.
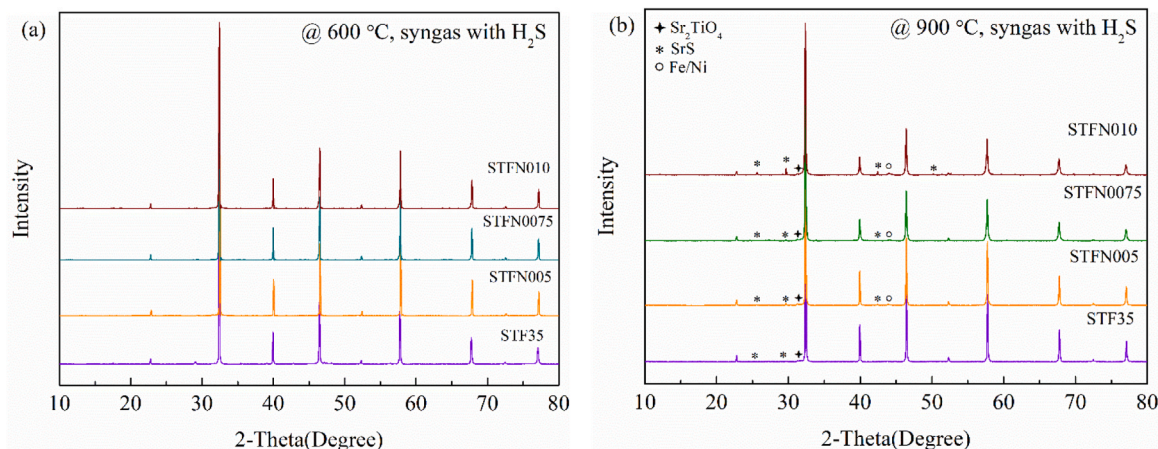

Fig. 9. XRD patterns of STF35 and STFN$_x$ samples annealed in syngas with H_2S at (a) 600 °C and (b) 900 °C.
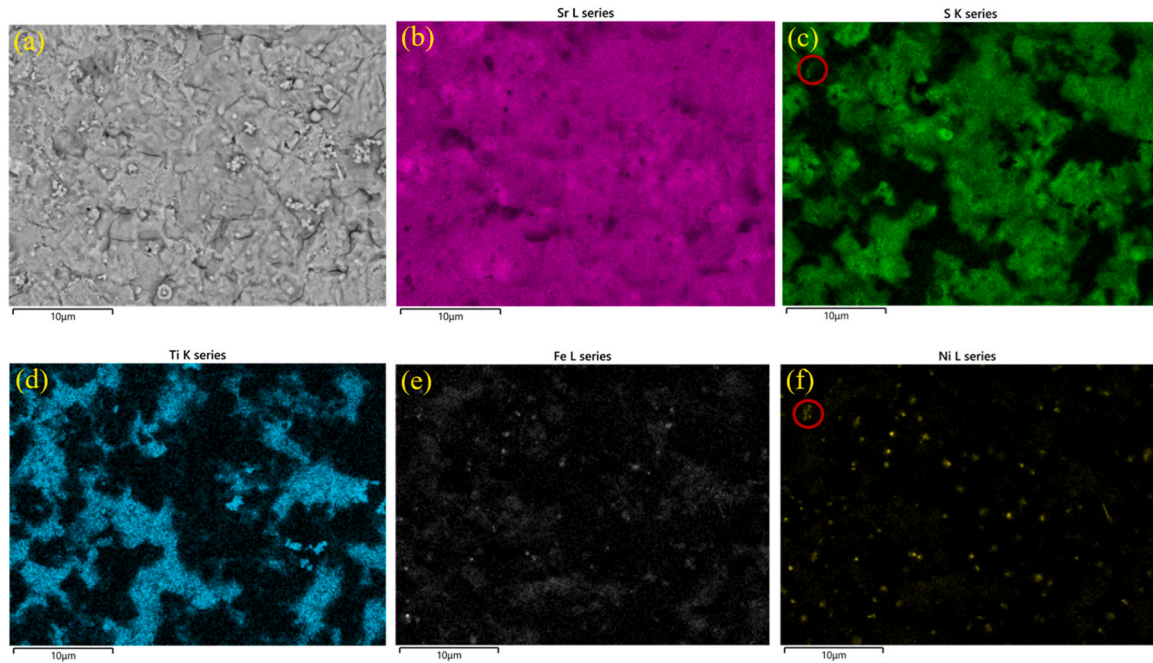
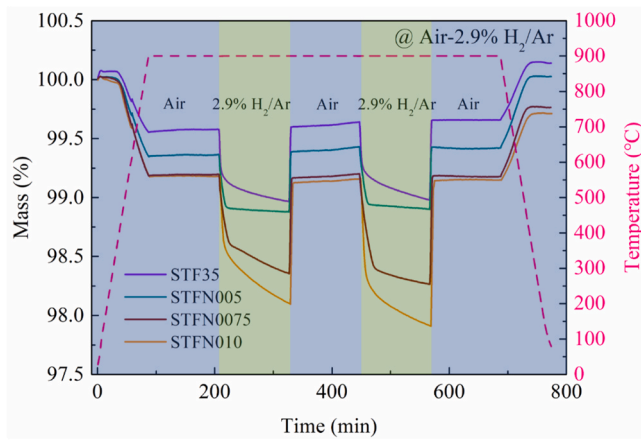**Fig. 10.** (a-f). SEM images and EDS mapping of STFN005 annealed at 900 °C in syngas with H$_2$S.

Fig. 11. Two-cycle TGA measurements of STF35 and STFN$_x$ in air and 2.9 % H$_2$/Ar atmospheres.

Fig. 12. XRD patterns of STF35 and STFN$_x$ after two-cycle TGA measurements.

phenomenon appears stronger at high temperature. It is also found on the surface of samples annealed at 900 °C by XRD patterns, which is consistent with the samples annealed in pure syngas. In addition, the excess SrO from the A site forms SrS in the H$_2$S-containing atmosphere and the remaining composition then forms Ruddlesden-Popper-like phases Sr$_2$TiO$_4$ in order to compensate for the remaining loss of A-site and cations. As Ni is easier to reduce than Fe[55], the intensity of SrS peaks on XRD patterns becomes higher with Ni increasing, indicating that the perovskite structure decomposes more severely and the stability of Ni-doped STF35 decreases with an increasing Ni content. As it is hard to distinguish between Ni and Ni$_2$S$_3$ by XRD patterns, SEM/EDS mapping were used to investigate the surface of materials after annealing (Fig. 10). A very small amount of NiS$_x$ (marked by red) and many Ni areas are clearly shown by EDS mapping. This is consistent with data calculated by FactSage software. The area where Sr and S are enriched at the same time is expected to be the SrS phase. Besides, the Fe/Ni metallic phase can also be detected by the mapping.

Two-cycle TGA measurements were carried out to compare the stability of the four samples in reducing atmosphere (Fig. 11). The mass loss
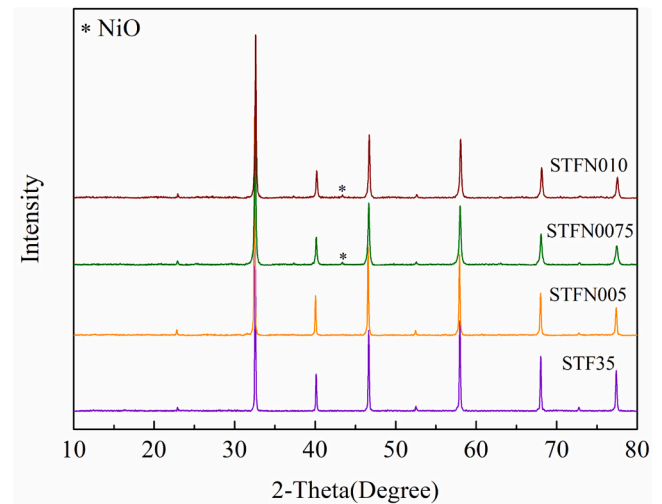
increases with Ni content increasing. For the first cycle, the mass loss of STF35 and STFN005 is close to each other (1.08 % and 1.12 %, respectively), but the degree strongly increases with 1.65 % for STFN0075 and 1.9 % for STFN010 after dwelling for 2 h in 2.9 % H$_2$/Ar at 900 °C. The mass loss further increases to 1.74 % for STFN0075 and 2.09 % for STFN010 during the second cycle, while that of STF35 and STFN005 still keeps a similar value as the first cycle (1.02 % and 1.10 %, respectively). XRD patterns shows that STF35 and STFN005 are still single phase after the two-cycle TGA measurements, while additional NiO peaks are found in STFN0075 and STFN010. This indicates that STF35 and STFN005 exhibit higher stability than STFN0075 and STFN010 in reducing atmosphere. Therefore, it can be concluded that the stability of STFN$_x$ will decrease with increasing Ni content and 5 % Ni-doped material STFN005 will not significantly reduce the material stability compared to STF35.

4. Conclusions

This work studied the influence of Ni doping on the B-site of STFN$_x$ with regard to structural and functional properties for its use in oxygen transport membranes. The results showed that Ni doping on the B-site can increase both electronic and ionic conductivities of STF35. The oxygen permeance of STFN$_x$ slightly varies with Ni concentration and is close to the benchmark LSCF6428. Fe and Ni exsolution phenomenon was clearly found on the surface of STF35 and STFN$_x$ after annealing in reducing atmospheres. All samples still possess the main peaks of perovskite evenly annealed in a very harsh condition, i.e. syngas with high H$_2$S contamination. The stability of STFN$_x$ decreased with increasing Ni content.

It is worth noting that even 5 % Ni-doped material STFN005 exhibits uniformly distributed Fe/Ni exsolution after annealing in a reducing atmosphere, which will benefit the catalytic performance in a membrane reactor. Two-cycle TGA measurements illustrate that STF35 and STFN005 exhibit higher stability than STFN0075 and STFN010 in a reducing atmosphere. Therefore, 5 % Ni doped STFN005 can be a promising material for POM in membrane reactors.

CRediT authorship contribution statement

Yuning Tang: Writing – review & editing, Writing – original draft, Software, Methodology, Investigation, Funding acquisition, Data curation, Conceptualization. **Doris Sebold:** Writing – review & editing, Investigation. **Arian Nijmeijer:** Writing – review & editing, Supervision, Resources. **Stefan Baumann:** Writing – review & editing, Supervision, Data curation. **Michael Müller:** Writing – review & editing, Methodology, Investigation, Data curation. **Olivier Guillon:** Writing – review & editing. **Wilhelm Albert Meulenberg:** Writing – review & editing, Supervision, Resources.

Declaration of Competing Interest

The authors declare that they have no known competing financial interests or personal relationships that could have appeared to influence the work reported in this paper.

Acknowledgements

References

[1] C. Salles, J. Fouletier, D. Marinha, M.-C. Steil, Determining the rate-limiting step during oxygen semi-permeation of CaTi0.9Fe0.1O3-δ oxygen transport membranes, J. Membr. Sci. 527 (2017) 191–197.

[2] A.H. Elbadawi, L. Ge, Z. Li, S. Liu, S. Wang, Z. Zhu, Catalytic partial oxidation of methane to syngas: review of perovskite catalysts and membrane reactors, Catal. Rev. 63 (1) (2021) 1–67.

[3] H. Chen, T. Zhu, X. Chen, Y. Bu, Q. Zhong, Sr(Ti,Fe)O3−δ Based Intermediate Temperature Solid Oxide Fuel Cell Anode with Self-precipitated (Ni,Fe) and Gd0.1Ce0.9O2−δ Nano Particles, J. Electrochem. Soc. 167 (16) (2020) 164507.

[4] X. Zhou, N. Yan, K.T. Chuang, J. Luo, Progress in La-doped SrTiO3(LST)-based anode materials for solid oxide fuel cells, RSC Adv. 4 (1) (2014) 118–131.

[5] Y. Teraoka, H.-M. Zhang, S. Furukawa, N. Yamazoe, Oxygen permeation through Perovskite-type oxides, Chem. Lett. 14 (11) (1985) 1743–1746.

[6] F. Schulze-Küppers, S. Baumann, W.A. Meulenberg, D. Stöver, H.P. Buchkremer, Manufacturing and performance of advanced supported Ba0.5Sr0.5Co0.8Fe0.2O3−δ (BSCF) oxygen transport membranes, J. Membr. Sci. 433 (2013) 121–125.

[7] C. Niedrig, S. Taufall, M. Burriel, W. Menesklou, S. Wagner, S. Baumann, E. Ivers-Tiffée, Thermal stability of the cubic phase in Ba0.5Sr0.5Co0.8Fe0.2O3-delta (BSCF)1, Solid State Ion. 197 (2011) 25–31.

[8] E.V. Artimonova, O.A. Savinskaya, A.P. Nemudry, Effect of B-site tungsten doping on structure and oxygen permeation properties of SrCo0.8Fe0.2O3−δ perovskite membranes, J. Eur. Ceram. Soc. 35 (8) (2015) 2343–2349.

[9] M. Kuhn, S. Hashimoto, K. Sato, K. Yashiro, J. Mizusaki, Oxygen nonstoichiometry and thermo-chemical stability of La0.6Sr0.4CoO3−, J. Solid State Chem. 197 (2013) 38–45.

[10] J. Ovenstone, J.-I. Jung, J.S. White, D.D. Edwards, S.T. Misture, Phase stability of BSCF in low oxygen partial pressures, J. Solid State Chem. 181 (3) (2008) 576–586.

[11] S.J. Xu, W.J. Thomson, Stability of La0.6Sr0.4Co0.2Fe0.8O3-δ perovskite membranes in reducing and nonreducing environments, Ind. Eng. Chem. Res. 37 (4) (1998) 1290–1299.

[12] M. Arnold, H. Wang, A. Feldhoff, Influence of CO2 on the oxygen permeation performance and the microstructure of perovskite-type (Ba0.5Sr0.5)(Co0.8Fe0.2) O3-?? membranes, J. Membr. Sci. 293 (2007) 44–52.

[13] Z. Wu, W. Jin, N. Xu, Oxygen permeability and stability of Al2O3-doped SrCo0.8Fe0.2O3−δ mixed conducting oxides, J. Membr. Sci. 279 (1-2) (2006) 320–327.

[14] A.L. Shaula, V.V. Kharton, J.C. Waerenborgh, D.P. Rojas, E.V. Tsipis, N. P. Vyshatko, M.V. Patrakeev, F.M.B. Marques, Transport properties and Mössbauer spectra of Fe-substituted La10−x(Si,Al)6O26 apatites, Mater. Res. Bull. 39 (6) (2004) 763–773.

[15] Y. Shen, F. Wang, X. Ma, T. He, SrCo 1− y Ti y O 3− δ as potential cathode materials for intermediate-temperature solid oxide fuel cells, Lancet 196 (2011) 7420–7425.

[16] O. Ravkina, T. Klande, A. Feldhoff, Investigation of Zr-doped BSCF perovskite membrane for oxygen separation in the intermediate temperature range, J. Solid State Chem. 201 (2013) 101–106.

[17] P. Haworth, S. Smart, J. Glasscock, J.C. Diniz da Costa, Yttrium doped BSCF membranes for oxygen separation, Sep. Purif. Technol. 81 (1) (2011) 88–93.

[18] L.-S. Unger, R. Ruhl, M. Meffert, C. Niedrig, W. Menesklou, S.F. Wagner, D. Gerthsen, H.J.M. Bouwmeester, E. Ivers-Tiffée, Yttrium doping of Ba 0.5 Sr 0.5 Co 0.8 Fe 0.2 O 3-δ part II: influence on oxygen transport and phase stability, J. Eur. Ceram. Soc. 38 (5) (2018) 2388–2395.

[19] F. Wang, T. Nakamura, K. Yashiro, J. Mizusaki, K. Amezawa, Effect of Nb doping on the chemical stability of BSCF-based solid solutions, Solid State Ion. 262 (2014) 719–723.

[20] G. Coffey, Electrochemical properties of lanthanum strontium aluminum ferrites for the oxygen reduction reaction, Solid State Ion. 158 (1-2) (2003) 1–9.

[21] M. Reichmann, P.M. Geffroy, J. Fouletier, N. Richet, P. Del Gallo, T. Chartier, Effect of cation substitution at the B site on the oxygen semi-permeation flux in La 0.5 Ba 0.5 Fe 0.7 B 0.3 O 3−δ dense perovskite membranes with B = Al, Co, Cu, Mg, Mn, Ni, Sn, Ti and Zn (part II), J. Power Sources 277 (2015) 17–25.

[22] X. Zhu, Q. Li, Y. He, Y. Cong, W. Yang, Oxygen permeation and partial oxidation of methane in dual-phase membrane reactors, J. Membr. Sci. 360 (1-2) (2010) 454–460.

[23] J.-J. Liu, S.-Q. Zhang, W.-D. Wang, J.-F. Gao, W. Liu, C.-S. Chen, Partial oxidation of methane in a Zr0.84Y0.16O1.92–La0.8Sr0.2Cr0.5Fe0.5O3−δ hollow fiber membrane reactor targeting solid oxide fuel cell applications, J. Power Sources 217 (2012) 287–290.

[24] F. Schulze-Küppers, S.F.P. ten Donkelaar, S. Baumann, P. Prigorodov, Y.J. Sohn, H. J.M. Bouwmeester, W.A. Meulenberg, O. Guillon, Structural and functional properties of SrTi 1−xFexO3−δ (0⩽x⩽1) for the use as oxygen transport membrane, Sep. Purif. Technol. 147 (2015) 414–421.

[25] V. Metlenko, W. Jung, S.R. Bishop, H.L. Tuller, R.A. De Souza, Oxygen diffusion and surface exchange in the mixed conducting oxides SrTi(1-y)Fe(y)O(3-delta), Phys. Chem. Chem. Phys. PCCP 18 (42) (2016) 29495–29505.

[26] V.V. Kharton, A.V. Kovalevsky, A.P. Viskup, J.R. Jurado, F.M. Figueiredo, E. N. Naumovich, J.R. Frade, Transport properties and thermal expansion of Sr0.97Ti1−FexO3− (x=0.2–0.8), J. Solid State Chem. 156 (2) (2001) 437–444.

[27] W. Jung, H.L. Tuller, Impedance study of SrTi 1−xFexO3−δ (x=0.05 to 0.80) mixed ionic-electronic conducting model cathode, Solid State Ion. 180 (11-13) (2009) 843–847.

[28] Y. Liu, S. Baumann, F. Schulze-Küppers, D.N. Mueller, O. Guillon, Co and Fe co-doping influence on functional properties of SrTiO3 for use as oxygen transport membranes, J. Eur. Ceram. Soc. 38 (15) (2018) 5058–5066.

[29] X. Li, H. Zhao, N. Xu, X. Zhou, C. Zhang, N. Chen, Electrical conduction behavior of La, Co co-doped SrTiO3 perovskite as anode material for solid oxide fuel cells, Int. J. Hydrog. Energy 34 (15) (2009) 6407–6414.

[30] Z. Zhao, R.V. Goncalves, S.K. Barman, E.J. Willard, E. Byle, R. Perry, Z. Wu, M. N. Huda, A.J. Moulé, F.E. Osterloh, Electronic structure basis for enhanced overall water splitting photocatalysis with aluminum doped SrTiO3 in natural sunlight, Energy Environ. Sci. 12 (4) (2019) 1385–1395.

[31] M.A.K.Y. Shah, Y. Lu, N. Mushtaq, M. Yousaf, S. Rauf, M.I. Asghar, P.D. Lund, B. Zhu, Perovskite Al-SrTiO3 semiconductor electrolyte with superionic conduction in ceramic fuel cells, Sustain. Energy Fuels 6 (16) (2022) 3794–3805.

[32] G. He, W. Liang, C.L. Tsai, X. Xia, S. Baumann, H. Jiang, W.A. Meulenberg, Chemical Environment-induced mixed conductivity of Titanate as a highly stable oxygen transport membrane, iScience 19 (2019) 955–964.

[33] M.L. Weber, M. Wilhelm, L. Jin, U. Breuer, R. Dittmann, R. Waser, O. Guillon, C. Lenser, F. Gunkel, Exsolution of embedded nanoparticles in defect engineered perovskite layers, ACS Nano 15 (3) (2021) 4546–4560.

[34] N. Xu, J. Zhang, S. Su, J. Feng, Z. Xu, Preparation and bifunctional properties of the A-site-deficient SrTi(0.3)Fe(0.6)Ni(0.1)O(3-delta) perovskite, RSC Adv. 12 (52) (2022) 33789–33800.

[35] T. Zhu, H.E. Troiani, L.V. Mogni, M. Han, S.A. Barnett, Ni-Substituted Sr(Ti,Fe)O3 SOFC Anodes: achieving high performance via metal alloy nanoparticle exsolution, Joule 2 (3) (2018) 478–496.

[36] D. Papargyriou, D.N. Miller, J.T. Sirr Irvine, Exsolution of Fe–Ni alloy nanoparticles from (La,Sr)(Cr,Fe,Ni)O3 perovskites as potential oxygen transport membrane catalysts for methane reforming, J. Mater. Chem. A 7 (26) (2019) 15812–15822.

[37] J. Wang, D. Kalaev, J. Yang, I. Waluyo, A. Hunt, J.T. Sadowski, H.L. Tuller, B. Yildiz, Fast surface oxygen release kinetics accelerate nanoparticle exsolution in perovskite oxides, J. Am. Chem. Soc. 145 (3) (2023) 1714–1727.

[38] Y. Liu, V. Motalov, S. Baumann, D. Sergeev, M. Müller, Y.J. Sohn, O. Guillon, Thermochemical stability of Fe- and co-functionalized perovskite-type SrTiO3 oxygen transport membrane materials in syngas conditions, J. Eur. Ceram. Soc. 39 (15) (2019) 4874–4881.

[39] E. Forster, D. van Holt, M.E. Ivanova, S. Baumann, W.A. Meulenberg, M. Müller, Stability of ceramic materials for H2 transport membranes in gasification environment under the influence of gas contaminants, J. Eur. Ceram. Soc. 36 (14) (2016) 3457–3464.

[40] D.T.T. Phuong, L.V. Hong, N.V. Minh, SrTi1-xNixO3 nanoparticles: synthesis and characterisation, Int. J. Nanotechnol. 8 (3-5) (2011) 312–323.

[41] A. Mizera, E. Drożdż, Studies on structural, redox and electrical properties of Ni-doped strontium titanate materials, Ceram. Int. 46 (15) (2020) 24635–24641.

[42] G.A. Alna'washi, A.M. Alsmadi, I. Bsoul, B. Salameh, G.M. Alzoubi, M. Shatnawi, S.M. Hamasha, S.H. Mahmood, Investigation on X-ray photoelectron spectroscopy, structural and low temperature magnetic properties of Ni-Ti co-substituted M-type strontium hexaferrites prepared by ball milling technique, Results Phys. 28 (2021) 104574.

[43] S. Molin, W. Lewandowska-Iwaniak, B. Kusz, M. Gazda, P. Jasinski, Structural and electrical properties of Sr(Ti, Fe)O3-δ materials for SOFC cathodes, J. Electroceram. 28 (1) (2012) 80–87.

[44] A. Rothschild, S.J. Litzelman, H.L. Tuller, W. Menesklou, T. Schneider, E. Ivers-Tiffée, Temperature-independent resistive oxygen sensors based on SrTi1−Fe O3−solid solutions, Sens. Actuators B Chem. 108 (1-2) (2005) 223–230.

[45] K. Shan, D. Dastan, Z.Z. Yi, M.K.A. Mohammed, X.T. Yin, A. Timoumi, A.S. Weidenbach, conductivity and aging behavior of Sr(Ti(0.6)Fe(0.4))(1-x) O(3-delta) mixed conductor materials, RSC Adv. 13 (13) (2023) 8683–8691.

[46] S.-L. Zhang, H. Wang, M.Y. Lu, A.-P. Zhang, L.V. Mogni, Q. Liu, C.-X. Li, C.-J. Li, S.A. Barnett, Cobalt-substituted SrTi0.3Fe0.7O3−δ: a stable high-performance oxygen electrode material for intermediate-temperature solid oxide electrochemical cells, Energy Environ. Sci. 11 (7) (2018) 1870–1879.

[47] M. Balaguer, S. Escolástico, J.M. Serra, Oxygen permeation and stability of CaTi0.73Fe0.18Mg0.09O3−δ oxygen-transport membrane, J. Membr. Sci. 524 (2017) 56–63.

[48] K. Li, H. Zhao, Y. Lu, Y. Ma, Z. Du, Z. Zhang, High CO2 tolerance oxygen permeation membranes BaFe0.95-xCa0.05TixO3-δ, J. Membr. Sci. 550 (2018) 302–312.

[49] T. Nagai, W. Ito, T. Sakon, Relationship between cation substitution and stability of perovskite structure in SrCoO3–δ-based mixed conductors, Solid State Ion. 177 (39) (2007) 3433–3444.

[50] P. Zeng, Z. Shao, S. Liu, Z.P. Xu, Influence of M cations on structural, thermal and electrical properties of new oxygen selective membranes based on SrCo0.95M0.05O3−δ perovskite, Sep. Purif. Technol. 67 (3) (2009) 304–311.

[51] J. Yang, H. Zhao, X. Liu, Y. Shen, L. Xu, Bismuth doping effects on the structure, electrical conductivity and oxygen permeability of Ba0.6Sr0.4Co0.7Fe0.3O3−δ ceramic membranes, Int. J. Hydrog. Energy 37 (17) (2012) 12694–12699.

[52] F. Yang, H. Zhao, J. Yang, M. Fang, Y. Lu, Z. Du, K. Świerczek, K. Zheng, Structure and oxygen permeability of BaCo0.7Fe0.3−In O3− ceramic membranes, J. Membr. Sci. 492 (2015) 559–567.

[53] Z. Wang, N. Dewangan, S. Das, M.H. Wai, S. Kawi, High oxygen permeable and CO2-tolerant SrCoxFe0.9-xNb0.1O3-δ (x = 0.1–0.8) perovskite membranes: behavior and mechanism, Sep. Purif. Technol. 201 (2018) 30–40.

[54] J.W. Stevenson, T.R. Armstrong, R.D. Carneim, L.R. Pederson, W.J. Weber, Electrochemical properties of mixed conducting perovskites La1 − x M x Co1 − y Fey O 3 − δ (M = Sr, Ba, Ca), J. Electrochem. Soc. 143 (9) (1996) 2722.

[55] T. Nakamura, G. Petzow, L.J. Gauckler, Stability of the perovskite phase LaBO3 (B = V, Cr, Mn, Fe, Co, Ni) in reducing atmosphere I. Experimental results, Mater. Res. Bull. 14 (5) (1979) 649–659.